Chinese Journal of Chemical Engineering 85 (2025) 228–237

Contents lists available at ScienceDirect

Chinese Journal of Chemical Engineering

journal homepage: www.elsevier.com/locate/CJChE

Full Length Article

Enhanced fluid-flow-field and electric-field synergistic interaction mechanism for lithium-ion separation in dilute solutions: A numerical analysis of electrochemically switched ion exchange system

Kangjun Ji [1], Jingxuan Yang [1,*], Xuefeng Zhang [1], Mengbo Zhao [1], Xiao Du [1], Xiaogang Hao [1,*], Abuliti Abudula [2], Guoqing Guan [2,3]

[1] College of Chemistry and Chemical Engineering, Taiyuan University of Technology, Taiyuan 030024, China
[2] Faculty of Science and Engineering, Hirosaki University, 3 Bunkyo-cho, Hirosaki, Aomori 036-8561, Japan
[3] Section of Renewable Energy, Institute of Regional Innovation (IRI), Hirosaki University, 3 Bunkyo-cho, Hirosaki, Aomori 036-8561, Japan

ARTICLE INFO

Article history:
Received 27 February 2025
Received in revised form
30 March 2025
Accepted 1 April 2025
Available online 24 April 2025

Keywords:
Electrochemically switched ion exchange
Mass transfer and separation
Synergistic effect
Fluid-flow-field
Fluidic dynamics
Electric-field

ABSTRACT

Electrochemically switched ion exchange (ESIX) is an effective technology for extracting high-value-added ions from dilute solutions. This study focuses on Li^+ extraction by employing a comprehensive model to analyze interaction between fluidic dynamics, electric field and ion transport. The model combines Butler–Volmer equation modified by electroactive site concentration, Nernst–Planck equation and Navier–Stokes equation. It is found that the chamber width affects solution phase resistance, thereby altering the potential distribution and influencing the current distribution within the membrane. A narrow chamber increases current density in the solid phase of the membrane, enhancing Li^+ extraction. The solution flow-field not only enhances convective transport but also increases the current density in the solid phase, promoting Li^+ extraction. There is a synergistic effect between fluid-flow-field and electric-field for ion separation, which is only significant when the chamber width is greater than 2 mm. The synergistic mechanism differs from that in the capacitive deionization system. Therefore, the performance decline caused by a wide chamber can be compensated for by increasing the fluid-flow rate, utilizing the synergistic effect between the fluid-flow-field and electric-field to optimize the lithium extraction efficiency in the ESIX system.

1. Introduction

Driven by carbon neutrality goals and policies, lithium-ion battery energy storage systems are increasing in many fields such as new energy vehicles and smart grids [1–3]. The market demand for lithium resources is surging at an annual increasing rate of 20% [4,5]. The current development of lithium resources is mainly concentrated in spodumene mines (hard rock mines) and salt-lake brines [6–8], with ore resources accounting for 30% and salt-lake resources for over 70%. Nearly 80% of China's lithium resources are found in the salt-lakes of Qinghai and Tibet [9,10].

The main methods for extracting lithium from salt-lake brines include precipitation [11–13], extraction [14–16], adsorption [17,18], electrodialysis [19], and electrochemical methods [20–22]. Among these, the electrochemical method stands out due to its high selectivity, low energy consumption, and high efficiency [23,24], aligning well with China's current carbon neutrality policy. The electrochemically switched ion exchange (ESIX) technology studied by our research group is a novel ion separation technology derived from the combination of electrochemical methods and traditional ion exchange techniques. This method involves depositing electroactive ion exchange functional materials onto a conductive substrate to form a nanoscale thin film and utilizing electrochemical methods to adjust the oxidation/reduction state of the film to control the insertion and release of ions [25,26], as shown in Fig. 1. Currently, the development of this technology mainly focuses on electroactive ion exchange functional membranes, including the design and development of membrane materials [27–29], potential loading methods [30], and membrane-phase electrochemical potential adjustment methods [31]. A theoretical model has also been established to describe the mass

* Corresponding authors.
E-mail addresses: yangjingxuan@tyut.edu.cn (J. Yang), xghao@tyut.edu.cn (X. Hao).

https://doi.org/10.1016/j.cjche.2025.04.004

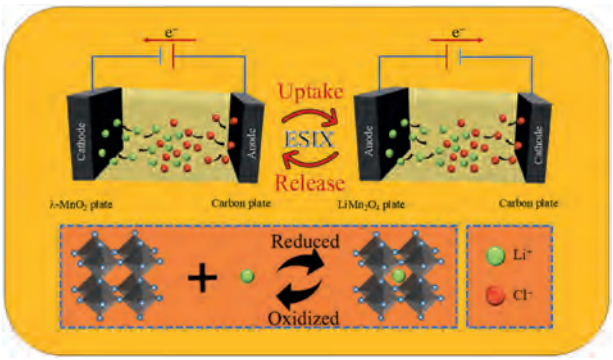

Fig. 1. Mechanism diagram in the ESIX process for Li^+ extraction.

transfer and electrochemical reaction processes within the membrane [32]. This technology demonstrates promising application prospects in the field of Li^+ recovery.

The process by which Li^+ ions enter the interior of an electrode material from solution and its reverse process are the main transport processes involved in the ESIX lithium extraction technology (as shown in Fig. 1). Theoretically, this transfer process is influenced by the fluid dynamics and electric field within the chamber. Zeng *et al.* [33] and Ye *et al.* [34] utilized ESIX technology to extract Cs^+ and Br^- ions, respectively. The experiments showed that when the chamber width was reduced from 8 to 2 mm, the extraction efficiencies for both Cs^+ and Br^- ions improved. As for the fluid flow rate, there exists a specific optimal value; when the fluid flow rate reaches this value, the ion extraction capacity can be maximized. Yu *et al.* [35] developed a method for extracting lithium ions from seawater using electrochemical methods, which is similar to the ESIX system. The study found that increasing the seawater flow rate can significantly enhance the extraction rate of Li^+ ions. Unfortunately, the aforementioned research did not delve into the mechanism by which flow and electric field synergistically promote ion separation.

The literature that provides a more in-depth elaboration on the convection-electric synergy mechanism is primarily found in the fields of capacitive deionization (CDI) and electrodialysis technology. Experiments by Sano *et al.* [36] demonstrate that fluid mixing in porous materials within an electrodialysis system can serve to reduce concentration polarization, which is crucial for enhancing the limiting current density. Mahendra *et al.* [37] and Lee *et al.* [38] measured the functional relationship between the limiting current density and velocity, as well as concentration, in an electrodialysis system. According to the literature [36–39], the mechanism underlying the flow-electric synergy effect is as follows: When the ion transport rate near the electrode surface cannot keep up with the ion adsorption rate driven by the electric field, the current density approaches its limiting value. At this point, severe concentration polarization occurs in the solution region near the electrode surface (the diffusion boundary layer), and the ion concentration near the electrode surface approaches zero, leading to insufficient ion supply and preventing the current from further increasing. Increasing the flow rate can reduce the thickness of the diffusion boundary layer, enhance ion transport, and thereby increase the limiting current density.

The ion adsorption behavior in the electroactive ion exchange material coated electrode is different from that in the CDI [32,40,41]. There are likely differences in the flow-electric synergy mechanism, but existing literature rarely addresses this issue. In this work, a mathematical model is established for the mass transfer phenomenon in the ESIX lithium extraction process to investigate the influence of fluid flow characteristics on lithium-ion extraction capacity. The emphasis is on exploring the mass transfer mechanisms behind the performance data. Especially the main mechanism of flow-electric synergy promoting ion adsorption. Providing a reference for the development of ESIX technology applied to lithium extraction from salt-lake brines.

2. Methods

2.1. ESIX system

The ESIX system simulated in this paper is a three-dimensional model. The ESIX system for lithium recovering consists of two electrodes and a chamber located between them, with a dilute solution of lithium chloride circulating between the chamber and a storage tank. The storage tank is equipped with strong stirring, ensuring that the incoming solution mixes uniformly with the solution in the tank. When the total processing volume remains constant, differences in chamber width will lead to variations in the overall volume of the chamber, which in turn will result in inconsistent amounts of residual liquid in the storage tank. As shown in Fig. 2, there are two electrodes, one of which is coated with λ-MnO_2 electroactive functional material for adsorbing Li^+ while a graphite electrode is chosen for electrostatic extraction of Cl^-.

Based on previous studies [33,34], the effects of width and flow rate are significant, therefore a research plan as shown in Table 1 has been developed.

2.2. Mass transfer kinetics model

2.2.1. λ-MnO_2 coated electrode

On the λ-MnO_2 coated electrode, the extraction equation for Li^+ is:

$$2\lambda\text{-}MnO_2 + Li^+ + e^- \rightarrow LiMn_2O_4$$

The following assumptions are made: the transport of water through the ion exchange membrane is negligible and ions on the membrane are immobile; only ions in the chamber can cross the membrane under the influence of voltage [42,43]. The current is uniformly applied to various positions on the λ-MnO_2 electrode. The extraction process on the λ-MnO_2 coated electrode follows the principles of mass balance and electroneutrality, described by [32]

$$\varepsilon\, \partial C_i / \partial t + \nabla \cdot J_i = R_i \tag{1}$$

$$\sum_i z_i c_i = 0 \tag{2}$$

where ε is the solid phase volume fraction, c_i ($mol \cdot L^{-1}$) is the concentration of ion i, J_i ($mol \cdot m^{-2} \cdot s^{-1}$) is the diffusion flux of ion i, R_i ($mol \cdot m^{-2} \cdot s^{-1}$) is the source term, with $R_i = -\nu_{Li}\alpha_v i_{loc}/nF$, representing the extraction rate of ion i, z_i is the valence of ion i.

The flux of ion i in the electrolyte is described by solving the Nernst–Planck equation [44,45].

$$J_i = -D_i \nabla c_i - z_i F D_i c_i \nabla \phi_l / RT + c_i u \tag{3}$$

The three terms on the right side represent the diffusion flux, migration flux, and convective flux of ion i, respectively. D_i ($m^2 \cdot s^{-1}$) is the diffusion coefficient of ion i, $F = 96485.33\ C \cdot mol^{-1}$ is the Faraday constant, ϕ_l (V) is the electrolyte potential, $R = 8.314\ J \cdot mol^{-1} \cdot K^{-1}$ is the molar gas constant, $T = 298$ K is the temperature, and u ($m \cdot s^{-1}$) is the fluid velocity.

Since the λ-MnO_2 coated membrane electrode is porous, the current density includes both the liquid-phase current density and the solid-phase current density, which can be expressed as follows [46].

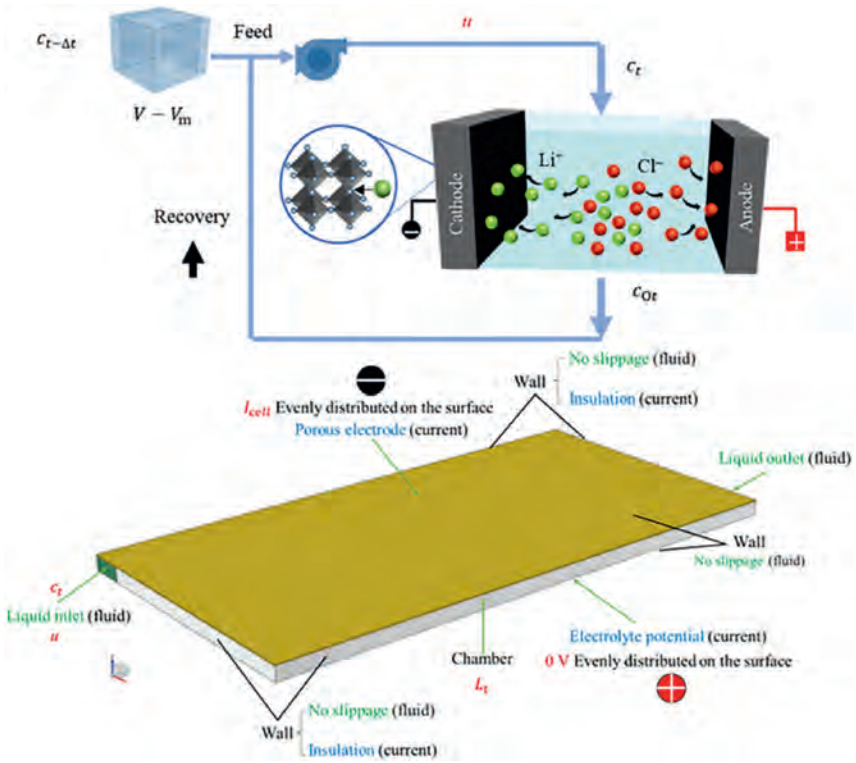

Fig. 2. ESIX system simulation process and structure.

$$i_{lm} = F\sum_i z_i J_i = F\sum_i z_i(-D_i\nabla c_i - z_i F D_i c_i \nabla\phi_{lm}/RT + c_i u) \quad (4)$$

$$i_{sm} = -\sigma_s\,\partial\phi_s/\partial x \quad (5)$$

where i_{lm} ($A\cdot m^{-2}$) is the liquid-phase current density in the λ-MnO_2 coated membrane electrode, ϕ_{lm} (V) is the liquid-phase potential of the λ-MnO_2 coated membrane electrode, i_{sm} ($A\cdot m^{-2}$) is the solid-phase current density in the λ-MnO_2 coated membrane electrode, σ_s ($S\cdot m^{-1}$) is the solid-phase conductivity in the λ-MnO_2 coated membrane electrode, and ϕ_s (V) is the solid-phase potential of the λ-MnO_2 coated membrane electrode. Meanwhile, i_s, the solid-phase current density, includes i_{loc}, the faradaic reaction current density, and i_{dl}, the double-layer current density.

Table 1
Variation in chamber width.

L_t/mm	V/ml	Q/ml·min^{-1}	A_m/mm^2	u/m·s^{-1}
0.5	30	9	2.5	0.06
		45		0.30
		90		0.60
		135		0.90
1.0	30	9	5.0	0.03
		45		0.15
		90		0.30
		135		0.60
1.5	30	9	7.5	0.02
		45		0.10
		90		0.20
		135		0.30

$$i_{sm} = i_{loc} + i_{dl} \quad (6)$$

The local faradaic current density is derived by introducing the electroactive site concentration through the Butler–Volmer equation [47]:

$$i_{loc} = i_0(\exp(\alpha_a F\eta/RT) - \exp(-\alpha_c F\eta/RT)) \quad (7)$$

$$i_0 = nFk_a^{\alpha_a}k_c^{\alpha_c}\left[(X - W_{ESC})\left(C_{Li}/C_{ref}\right)\right]^{0.5}(W_{ESC})^{0.5} \quad (8)$$

$$\eta = \phi_s - \phi_l - E_{eq} \quad (9)$$

$$dW_{ESC}/dt = \alpha_v i_{loc}/nF \quad (10)$$

where i_{loc} ($A\cdot m^{-2}$) is the local faradaic current density, i_0 ($A\cdot m^{-2}$) is the exchange current density, α_a and α_c are the anodic and cathodic transfer coefficients, respectively, with $\alpha_a = \alpha_c = 0.5$, k_a and k_c ($m\cdot s^{-1}$) are the kinetic rate constants for oxidation and reduction, respectively. X ($mol\cdot m^{-3}$) is the total concentration of electroactive sites, W_{ESC} ($mol\cdot m^{-3}$) is the concentration of activated electroactive sites, C_{Li} ($mol\cdot m^{-3}$) is the concentration of Li^+ in the chamber, C_{ref} ($mol\cdot L^{-1}$) is the reference concentration, which is 1 $mol\cdot L^{-1}$, E_{eq} (V) is the equilibrium potential of λ-MnO_2 in the LiCl solution, and α_v (m^{-1}) is the specific active surface area in the λ-MnO_2 coated membrane electrode.

The double-layer current density, i_{dl}, refers to the charging and discharging current of the double layer, also known as non-Faradaic current, and its expression is:

$$i_{dl} = C_{dl}\partial\phi_s/\partial t \tag{11}$$

where C_{dl} ($F\cdot m^{-2}$) is the double-layer capacitance.

2.2.2. Graphite electrode

In a graphite electrode, charge transfer is accomplished through electrostatic extraction. The extraction process involves [47].

$$W_e + W_{Cl} = 0 \tag{12}$$

where W_e ($mol\cdot m^{-3}$) is the electron charge concentration on the graphite surface, and W_{Cl} ($mol\cdot m^{-3}$) is the charge concentration of Cl^- ions.

2.2.3. Chamber

The electrolyte solution in the chamber follows charge conservation and mass conservation, and since the electrolyte solution does not participate in the reaction, there are no reaction source terms. Therefore, the mass conservation equation (continuity equation) and charge conservation equation for the electrolyte are as follows [48,49]:

$$\partial C_{Li} / \partial t + \nabla\cdot J_{Li} = 0 \tag{13}$$

$$\sum_i z_i c_i = 0 \tag{14}$$

Since the electrolyte solution is entirely composed of electrolytes, the total current is solely composed of the electrolyte current, and there is no solid phase present.

$$i_l = F\sum_i z_i J_i = F\sum_i z_i(- D_i\nabla c_i - z_i F D_i c_i \nabla\phi_l / RT + c_i u) \tag{15}$$

and

$$i_l = -\sigma_l \Delta\phi_l / L_t \tag{16}$$

$$i_s = 0 \tag{17}$$

where σ_l ($S\cdot m^{-1}$) is the liquid-phase conductivity.

2.3. Charge conservation in the ESIX system

Both experiments and simulations are conducted with a constant current λ-MnO_2 coated electrode while the electrostatic potential of the graphite electrode is set to 0 V. The constant current I_{cell} is the sum of the solid-phase current density i_s in the λ-MnO_2 coated electrode and the liquid-phase current density i_l in the electrolyte [46,50].

$$I_{cell} = i_s + i_l \tag{18}$$

and

$$\nabla i_l = -\nabla i_s \tag{19}$$

2.4. Flow model of dilute solution

The momentum equation for the electrolyte solution is [42,51]:

$$\rho(u\cdot\nabla)u = -\nabla P + \mu\nabla^2 u + g \tag{20}$$

where ρ ($kg\cdot m^{-3}$) is the fluid density, P (Pa) is the pressure, μ (Pa · s) is the dynamic viscosity, and g ($N\cdot m^{-3}$) is the gravitational body force term.

Assuming the fluid is incompressible, the continuity equation is:

$$\nabla\cdot u = 0 \tag{21}$$

2.5. Initial conditions

At $t = 0$:

In the chamber: $c_{Li} = c_{Cl} = 49.2\ mol\cdot m^{-3}$, $\phi_l = 0$ V.

On the λ-MnO_2 coated electrode: $W_{ESC} = 0\ mol\cdot m^{-3}$, $\phi_s = \phi_l = 0$ V.

On the graphite electrode: $W_e = 0\ mol\cdot m^{-3}$, $W_{Cl} = -42.9\ mol\cdot m^{-3}$.

2.6. Boundary conditions

The inlet boundary is set as the velocity inlet with the velocity values shown in Table 1. The outlet boundary condition is set as the pressure outlet with a static pressure value of 0. For the flow equations, a no-slip boundary condition is applied at the interface between the liquid and the membrane phase [52].

Assuming that the solution flowing out of the ESIX system can mix rapidly and uniformly with the solution stored in the tank, the concentration of the mixed solution is assigned to the inlet as a boundary condition. Therefore, the inlet solution concentration varies with time and is calculated using the following equation:

$$c_t = ((V - V_m)c_{t-\Delta t} + u\Delta t A c_{Ot}) / ((V - V_m) + u\Delta t A) \tag{22}$$

where c_t ($mol\cdot m^{-3}$) is the inlet LiCl concentration at time t (s), $c_{t-\Delta t}$ ($mol\cdot m^{-3}$) is the inlet LiCl concentration at time $t-\Delta t$, c_{Ot} is the outlet LiCl concentration at time t, V_m (ml) is the chamber volume, V (ml) is the total processing volume, u ($m\cdot s^{-1}$) is the average flow velocity, Δt (s) is the iteration time and A (mm^2) is the membrane area.

2.7. Solution

The aforementioned system of equations can be solved using the finite element method. The computation process is in transient mode. Since the Reynolds number (Re) corresponding to the maximum flow rate is 1605.6, which is below the critical value of 2000, we choose a laminar flow interface to calculate the fluid dynamics problem. The electrochemical module is calculated using a cubic current distribution, boundary ordinary differential equations, and differential-algebraic equations interfaces. The

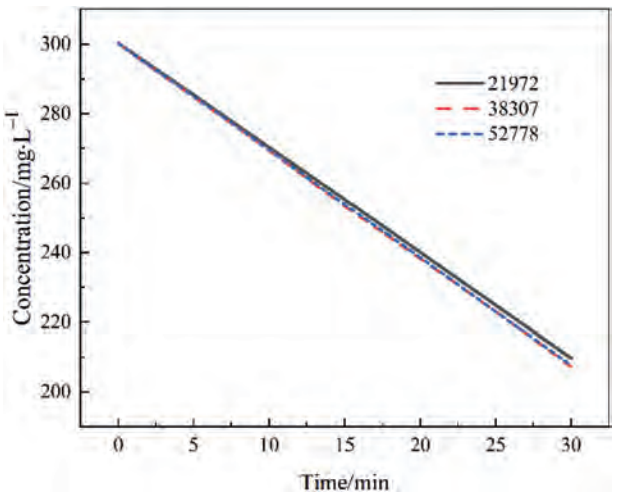

Fig. 3. Mesh independence verification.

Table 2
Relative parameters used in experimental model validation.

Parameter	Value	Reference
Flow rate, Q/ml·min^{-1}	45	
Speed, u/m·s^{-1}	0.10	
Constant current for extraction, I_{cell}/A· m^{-2}	1	
Chamber width, L_t/mm	0.5,1.0,1.5	
Inlet cross-sectional area, A_m/mm^2	2.5,5,7.5	
Length of λ-MnO_2 electrode, L_l/cm	8	
Width of λ-MnO_2 electrode, L_w/cm	4	
Thickness of λ-MnO_2 electrode, L_{film}/mm	0.2	
Diffusion coefficient of Li^+, D_{Li}/m^2·s^{-1}	9.9×10^{-10}	[48,49]
Diffusion coefficient of Cl^-, D_{Cl}/m^2·s^{-1}	1.98×10^{-9}	[48,49]
Initial concentration of LiCl, C_0/mol·m^{-3}	42.9	
Solid-phase conductivity, σ_s/S·m^{-1}	12.7	
Faraday constant, F/C·mol^{-1}	96485.33	
Molar gas constant, R/J·mol^{-1}· K^{-1}	8.314	
Temperature, T/K	298	
Anodic and cathodic faradaic transfer coefficient, $\alpha_a = \alpha_c$	0.5	
Specific rate constant of faradaic reaction, $k_a = k_c$/m·s^{-1}	10^{-11}	
Electrolyte reference concentration, C_{ref}/mol·L^{-1}	1	
Total concentration of electroactive sites, X/mol·m^{-3}	25000	
Specific active surface area, α_v/m^{-1}	10^7	
Stoichiometric number of Li^+ extraction reaction, ν_{Li}	−1	
The charge number of Li^+, z_{Li}	1	
The charge number of Cl^-, z_{Cl}	−1	
Volume fraction of solid phase, ε	0.5	
Chamber volume, V_m/ml	1.6,3.2,4.8	
Processing capacity or volume, V/ml	30	
Dynamic viscosity, μ/Pa·s	0.75	
Membrane area, A/mm^2	32	
Double-layer capacitance, C_{dl}/F·m^{-2}	0.8	

extraction process of Li^+ is quantitatively described by introducing changes in the concentration of electroactive sites [45]. A free tetrahedral mesh is used, with mesh refinement near the boundaries, inlets, and outlets. To ensure that the quality and accuracy of the simulation results are not affected by the number of meshes, three different mesh quantities of 21972, 38307, and 52778 are used to discretize the computational domain. The results are shown in Fig. 3. To obtain more accurate results while improving computational efficiency, the case with a mesh count of 38307 is selected for the simulation. Table 2 summarizes the descriptions and values of all parameters used in the simulation.

3. Results and Discussion

3.1. Model validation

The model was validated using the experimental method for Li^+ extraction using the ESIX system by Zhang *et al.* [9] from our research group. To fully verify the effectiveness of the mathematical model, the input parameters used in the model were all derived from experimental parameters. As can be seen from Fig. 4, the simulation results align with the experimental data within the error range.

3.2. Li^+ extraction performance

To investigate the impact of chamber width on the Li^+ extraction performance, the specific scheme by changing the chamber width is as shown in Table 1.

Under a flow rate of 45 ml·min^{-1}, the influence of chamber width on the Li^+ extraction rate is shown in Fig. 5(a). From the provided data, we can observe the impact of chamber width on Li^+ extraction rate in both simulated and experimental conditions. In

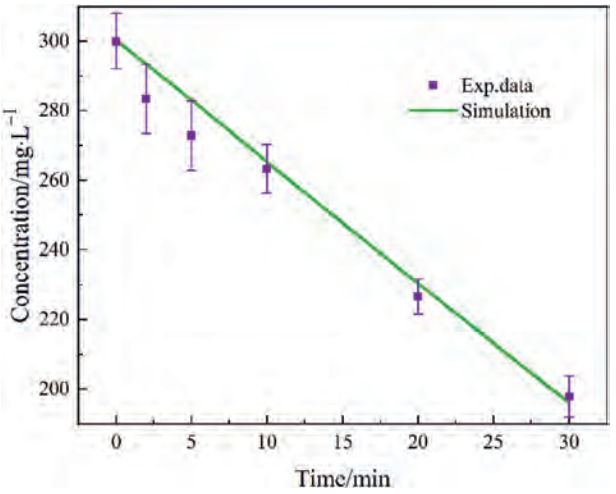

Fig. 4. Comparisons of calculation results with experimental data.

the simulated scenario: when the chamber width is 0.5 mm, the Li^+ concentration drops from 300 to 38 mg·L^{-1}; when the chamber width is 1.5 mm, the Li^+ concentration decreases from 300 to 196 mg·L^{-1}. It can be inferred that as the chamber width decreases from 1.5 to 0.5 mm, the Li^+ extraction rate increases by 1.52 times. In the experimental situation: with a chamber width of 0.5 mm, the Li^+ concentration reduces from 300.0 to 247.5 mg·L^{-1} while with a chamber width of 1.5 mm, the Li^+ concentration falls from 300.7 to 284.2 mg·L^{-1}. It is evident that as the chamber width narrows from 1.5 to 0.5 mm, the Li^+ extraction rate increases by 2.18 times. Both the simulated and experimental results indicate that reducing the chamber width significantly enhances the extraction of Li^+.

The experiment shown in Fig. 4 was conducted in a lithium chloride solution, and one can see that its experimental results are highly consistent with the simulation predictions. In contrast, the experiment in Fig. 5(a) was carried out in brine under the same environmental condition, and it is found that there are certain numerical deviations between the experimental data and simulation results. Nevertheless, there is still a certain similarity in the trend of the two sets of data. This deviation is attributed to the fact that the current simulation model primarily focuses on the separation effect in a pure solution environment and has not fully incorporated the characteristics of the complex brine system, which constitutes a limitation of the current mathematical model. In light of this, we plan to further optimize and improve the model based on the existing simulation framework in future work to more accurately reflect the separation process under brine conditions.

Since the flow rate is the same, different chamber widths correspond to different flow velocities. To analyze whether the difference in Li^+ extraction rate is due to the change in flow velocity, four flow rates were set for each of the three chamber widths to study the effect of flow velocity. The results are shown in Fig. 5(b), (c) and (d) which indicate that in a wider chamber, the flow rate has a significant impact on Li^+ extraction rate whereas in a narrower chamber, the influence of flow rate is very slight. When the chamber width is 1.5 mm, increasing the flow rate from 9 to 135 ml·min^{-1} results in a 33.3% increase in Li^+ extraction rate; whereas when the chamber width is reduced to 0.5 mm, with the same increase in flow rate, the Li^+ extraction rate only increases by 0.4%. On the other hand, there is a marginal effect of flow rate on enhancing Li^+ extraction rate. For a chamber with a width of 1.5 mm, the Li^+ extraction capacities at flow rates of 90 and 135 ml·min^{-1} are almost the same.

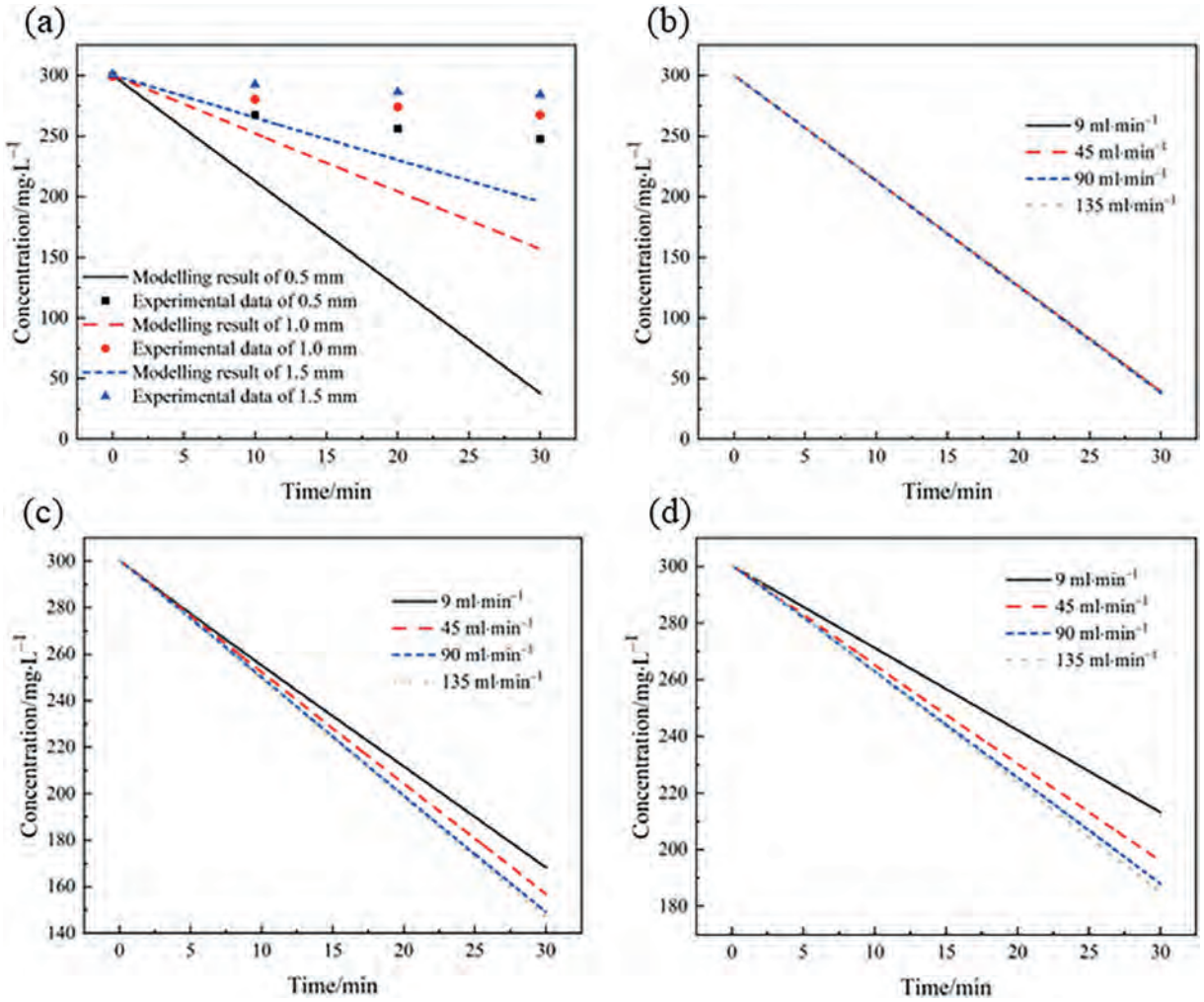

Fig. 5. Li^{+} extraction rates with (a) varying chamber width at 45 ml·min^{-1}; (b) varying flow rate at 0.5 mm; (c) varying flow rate at 1.0 mm; (d) varying flow rate at 1.5 mm.

More importantly, even at the maximum flow rate, the Li^{+} concentration in the outlet solution of the 1.5 mm-wide chamber is still much higher than that of the 0.5 mm-wide chamber. Therefore, the difference in Li^{+} extraction rate at different widths is not mainly due to the influence of flow velocity. In the ESIX system, there is an electric field on both sides of the solution, so it is necessary to explore the voltammetric characteristics of the system to investigate the causes of the aforementioned phenomena.

3.3. Analysis of the voltammetric characteristics of the system

Fig. 6 shows the potential difference across the chamber. At the initial moment, the potential differences across the three chambers exhibit a ratio of 1:2:3, which is the same as the ratio of the chamber thicknesses. The initial ion concentration and conductivity of the solution are the same, so the resistance in the direction of the chamber thickness is proportional to the width. Since the system operates with a constant current, according to Ohm's law, the potential difference across the chamber is proportional to the thickness. As the electro-extraction process progresses, the potential difference across the chamber is no longer proportional to the thickness, but it remains that the greater the thickness is, the higher the potential difference is.

Fig. 7 presents the voltammetric characteristics of the membrane phase and the solution phase at the initial moment. This study focuses on lithium-ion extraction and simplifies the electrode as electrode plate, maintaining a potential of 0. When the chamber width is reduced from 1.5 to 0.5 mm, the potential

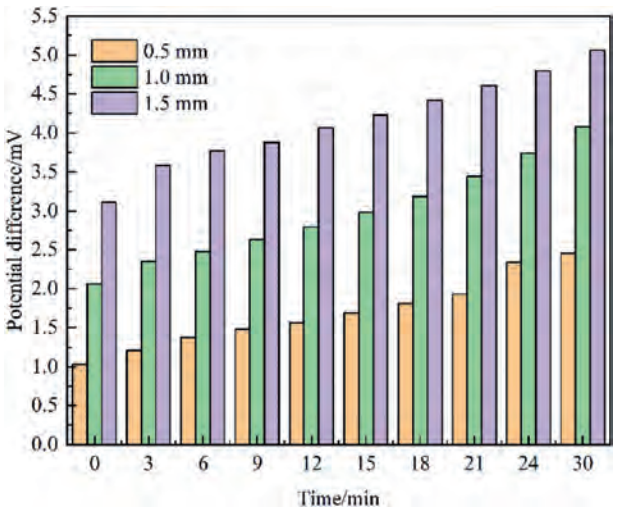

Fig. 6. Potential differences across the chambers for different chamber widths.

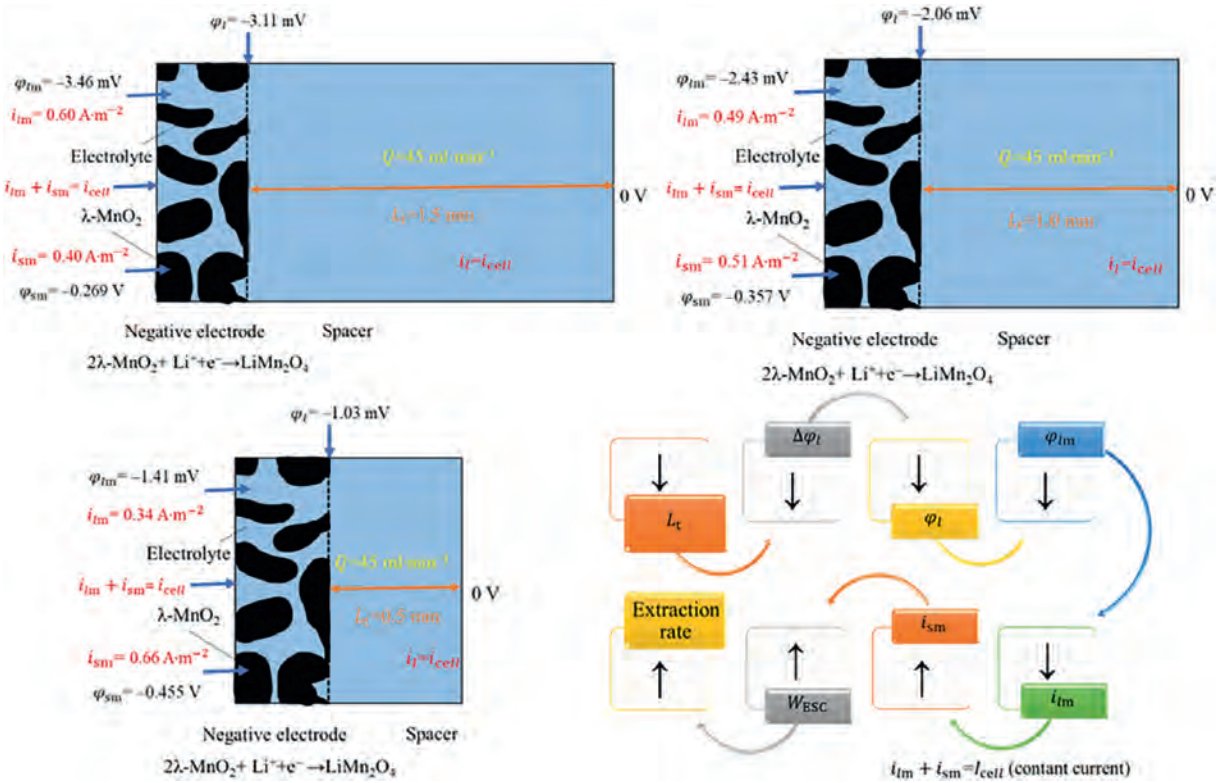

Fig. 7. Relationship between potential and current in the membrane phase and solution phase.

difference decreases from 3.11 to 1.03 mV, representing a reduction of approximately 67%. At the same time, the potential at the interface between the membrane electrode and the solution also decreases by a corresponding amount. Considering that the thickness of the membrane electrode is only 200 μm, which is much smaller than the width of the chamber, the difference between the liquid-phase potential in the membrane electrode and the potential of the solution at the interface is very small. Based on this change, when the chamber width is reduced from 1.5 to 0.5 mm, the liquid-phase potential in the membrane electrode decreases by approximately 59%. In a porous electrode system, this reduction in the liquid-phase potential of the membrane electrode leads to a decrease in the liquid-phase current density (according to Eq. (4)), specifically by approximately 43%. Since the system operates under the constant current condition, the decrease in liquid-phase current density prompts an increase in solid-phase current density (according to Eq. (18)), resulting in a solid-phase current density increase of approximately 65%. According to the Li^+ extraction reaction equation, the electroactive material λ-MnO_2 acquires Li^+ extraction capability only in the presence of free electrons. Therefore, an increase in solid phase current density implies that more free electrons are distributed in the porous electrode material, activating more electroactive substances and forming a stronger extraction rate.

In summary, the chamber structure determines the resistance of the solution phase, which affects the distribution of potential between the membrane phase and the solution phase. This influence propagates to the membrane phase, altering the distribution of current between the solid and liquid phases within the membrane. This is the key mechanism by which the chamber structure significantly modulates the Li^+ extraction capability.

3.4. Synergistic effect by fluid-field-flow

3.4.1. Formation mechanism

The reason for the enhanced Li^+ extraction performance with the increase in fluid flow rate, as shown in Fig. 6, can be reasonably explained by the dynamic effect of solution flow on the voltammetric characteristics of the membrane phase.

As shown in Fig. 8, the potential difference decreases with the increase in fluid flow rate in chambers of all three widths. The essence of solution current is ion transport, and the ion transport mechanism includes the effects of concentration diffusion, electromigration, and convective transport (Eq. (3)). When the system operates under the constant current condition with the total rate of ion transport remaining unchanged, increasing the flow rate enhances the convective transport, which necessarily leads to a decrease in other transport mechanisms. At the initial moment, ions are uniformly distributed in the solution with no concentration diffusion. Therefore, the only way to balance the enhanced convective transport caused by the increased flow rate is to reduce the electromigration rate by decreasing the potential difference. Based on the analysis in Section 3.3, the reduction in the potential difference across the chamber will alter the distribution of the liquid-phase and solid-phase potentials in the membrane, increase the solid-phase current density, activate more electroactive materials, and improve the Li^+ extraction rate. The enhancement of fluid dynamics within the chamber not only strengthens the convective transport of ions in the solution phase but also increases the solid-phase current density in the membrane, promoting Li^+ extraction. In the ESIX system, there exists a synergistic effect between fluid-flow-field and electric-field for the enhancement of mass transfer as well as separation processes. This is significantly different from the flow-electric synergy effect in CDI systems.

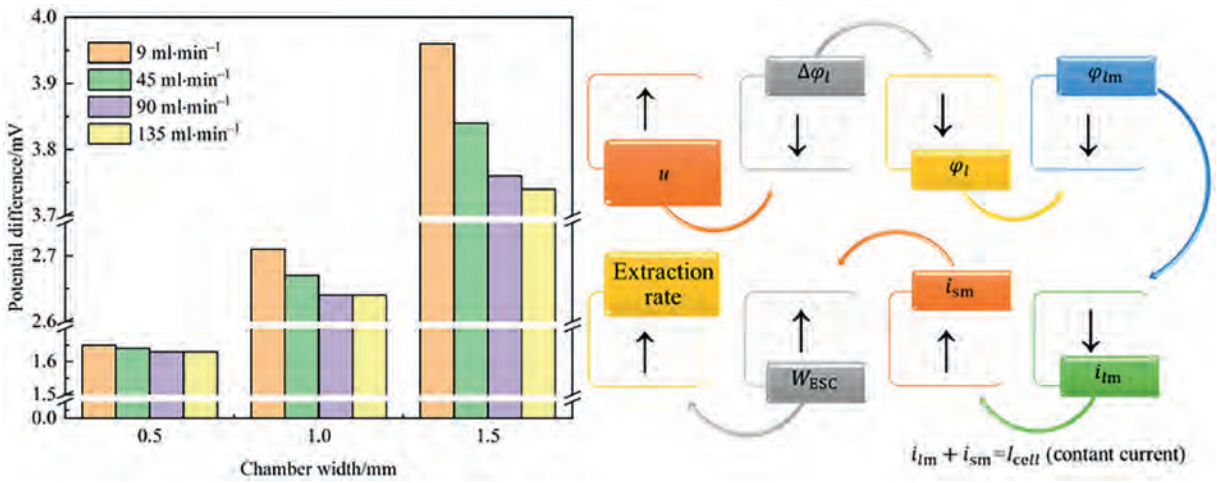

Fig. 8. Potential differences across the chambers under different chamber widths and fluid flow rates (2 min).

In CDI systems, the field-flow synergy effect is mainly manifested in the calculation of the limiting current density, i_{lim} ($A \cdot m^{-2}$)

$$i_{lim} = aCu^b \tag{23}$$

where C ($mol \cdot L^{-1}$) is the concentration of the diluate, u ($m \cdot s^{-1}$) is the flow velocity of the solution, and a and b are the characteristic constants for a given.

Where an increase in flow rate enhances the limiting current density i_{lim}, thereby improving ion extraction efficiency. When the current approaches its limiting value, the ion concentration at the electrode/membrane surface tends to zero, leading to mass transfer rate limitations. By increasing the flow rate, the thickness of the diffusion boundary layer can be reduced, enhancing convective mass transfer of bulk ions to the interface, thereby increasing i_{lim} and mitigating the concentration polarization phenomenon [36–39].

The ion adsorption behavior in the electroactive ion exchange material coated electrode is different from that in the CDI [32,40,41]. In the ESIX system, there exists a Donnan equilibrium at the solution–membrane–electrode interface, and the ion concentration does not become too low to cause a bottleneck in the mass transfer rate. Therefore, the increase in flow rate alters the potential distribution at the solution–membrane–electrode interface, thereby changing the Donnan equilibrium state, rather than due to the influence of flow on the boundary layer. In terms of the formation mechanism, the flow-electric synergy effect in the ESIX system differs significantly from that in the CDI system.

3.4.2. Application

The influence of fluid flow rate on the potential difference between the two sides of the chamber is shown in Fig. 8. When the chamber width is 1.5 mm, as the flow rate increases from 9 to 135 ml·min^{-1}, the potential difference between the two ends of the chamber decreases by 5.6%. Correspondingly, the Li^+ extraction rate increases by 33.3%. When the chamber width is reduced to 0.5 mm, with the same increase in fluid flow rate, the potential difference between the two ends of the chamber decreases by only 1.2%, and the Li^+ extraction rate remains basically unchanged. The synergistic effect of fluid-flow-field and electric field becomes more significant as the chamber width increases.

To analyze the conditions under which the synergistic effect of fluid-flow-field and electric field occurs, the chamber width studied was extended to 8 mm, with the flow rate range as indicated in Table 1. As shown in Fig. 9(b), within the chamber width range of 0.5 to 1.5 mm, the contours of extraction rates are almost parallel to the vertical axis. Taking the chamber width of 1 mm as an example,

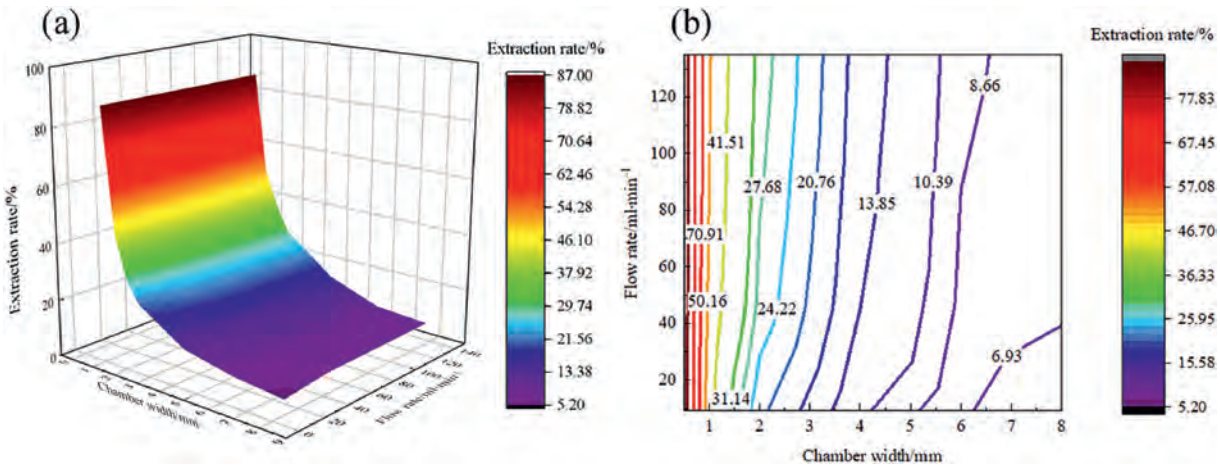

Fig. 9. Variations of chamber type and flow extraction rate: (a) 3D multi-response surface plot; (b) 2D contour plot.

when the flow rate is increased from 9 to 135 ml·min^{-1}, the increase in Li^+ extraction rate is only 16%, indicating that the synergistic effect of fluid-flow-field and electric field is not significant. When the chamber width increases to 2 mm or more, the contours of extraction rates are no longer parallel to the vertical axis. Taking the chamber width of 2 mm as an example, when the flow rate is increased from 9 to 135 ml·min^{-1}, the Li^+ extraction rate increases significantly by about 36%. Therefore, the synergistic effect of fluid-flow-field and electric field is significant only when the chamber width is greater than 2 mm.

As shown in Fig. 9(a), when the chamber width is greater than 2 mm, the loss of Li^+ extraction capability exceeds 50%. Ye *et al.* [34] conducted research on the performance of ESIX systems for extracting Br^- and proposed that a chamber thickness of 2 mm is optimal. While narrowing the chamber width can improve adsorption performance, it may easily lead to the contact of two electrodes, causing a short circuit. This poses hidden risk to the long-term safety and stable operation of the device. Based on the analysis of the synergistic effect of fluidic dynamics and electric field in this study, increasing the flow rate can partially compensate for the performance loss caused by the increase in chamber width. According to the calculations in this study, when the chamber width is increased to 3 mm and the flow rate is increased to 135 ml·min^{-1}, the Li^+ extraction rate is approximately 21.7%; whereas with a chamber width of 2 mm and a flow rate of 9 ml·min^{-1}, the Li^+ extraction rate is about 20.7%. That is, under these two conditions, the performances of the ESIX devices are comparable.

4. Conclusions

In this study, a comprehensive model was set up to analyze interaction between fluidic dynamics, electric field and ion transport Li^+ extraction by the ESIX system. The following results were obtained.

(1) The width of the dilute solution chamber is a key factor affecting the lithium extraction performance of the ESIX system. The influence mechanism lies in the fact that the chamber width determines the resistance of the solution phase, which affects the distribution of potential between the membrane phase and the solution phase. This influence propagates to the membrane phase, altering the distribution of currents between the solid and liquid phases within the membrane. The smaller the chamber width is, the higher the current density in the solid phase of the membrane is, and the stronger the Li^+ extraction capability is.

(2) In the ESIX system, there is a synergistic effect between fluidic dynamics and electric field for enhancing the mass transfer and separation processes. The increase in fluid flow rate within the chamber not only enhances the convective transport of ions in the solution phase but also increases the current density in the solid phase of the membrane, promoting Li^+ extraction.

(3) The flow-electric synergy mechanism in the ESIX system is significantly different from that in the CDI system. In the CDI system, the field-flow synergy effect is mainly manifested in the influence of flow on the limiting current density, whereas in the ESIX system, it is manifested in the influence of flow on the potential difference.

(4) The synergistic effect of fluidic dynamics and electric field is only significant when the chamber width is greater than 2 mm. Utilizing this synergistic effect, in the design of the ESIX process, the flow rate of the dilute solution can be increased to partially compensate for the decrease in lithium extraction capacity caused by an increase in chamber width.

CRediT Authorship Contribution Statement

Kangjun Ji: Writing – review & editing, Writing – original draft, Visualization, Methodology, Investigation. Jingxuan Yang: Writing – review & editing, Writing – original draft, Visualization, Methodology, Investigation, Conceptualization. Xuefeng Zhang: Software, Formal analysis. Mengbo Zhao: Investigation. Xiao Du: Investigation. Xiaogang Hao: Supervision, Project administration, Funding acquisition, Formal analysis, Conceptualization. Abuliti Abudula: Supervision. Guoqing Guan: Supervision.

Declaration of Competing Interest

The authors declare that they have no known competing financial interests or personal relationships that could have appeared to influence the work reported in this paper.

Acknowledgements

This work is supported by the National Natural Science Foundation of China (22378285, 92475117 and U21A20303).

References

[1] P. Afzali, E. Gibertini, L. Magagnin, Improved plating/stripping in anode-free lithium metal batteries through electrodeposition of lithiophilic zinc thin films, *Electrochim. Acta* 488 (2024) 144190.
[2] V.V.K. Lanjapalli, F.J. Lin, S. Liou, S. Hosseini, C.L. Huang, Y.S. Chen, Y.Y. Li, Semi-infused lithium anode for advanced Li metal batteries, *Electrochim. Acta* 410 (2022) 139976.
[3] P.B. Samarasingha, M.T. Lee, M. Valvo, Reactive surface coating of metallic lithium and its role in rechargeable lithium metal batteries, *Electrochim. Acta* 397 (2021) 139270.
[4] B. Swain, Recovery and recycling of lithium: a review, *Sep. Purif. Technol.* 172 (2017) 388–403.
[5] Z.W. Zhao, G. Liu, H. Jia, L.H. He, Sandwiched liquid-membrane electrodialysis: lithium selective recovery from salt lake brines with high Mg/Li ratio, *J. Membr. Sci.* 596 (2020) 117685.
[6] M. Zhang, N. Garcia-Araez, Core-shell structured $LiFePO_4$/C nanocomposite battery material for lithium production from brines, *Electrochim. Acta* 499 (2024) 144686.
[7] M. Faheem, R. Alam, A. Alhajaj, L.D. Zou, Recovery of lithium by pseudocapacitive electrodes in capacitive deionization, *Electrochim. Acta* 489 (2024) 144267.
[8] S. Sun, Y.F. Deng, J. Chen, D. Zou, Y.X. Han, M.Y. Liu, Recovery of lithium from the desorption solutions of salt lakes using β-diketone synergistic extraction system, *Sep. Purif. Technol.* 354 (2025) 128748.
[9] Z. Zhang, Y.P. He, H.D. Sun, R.Z. Zhang, Z.P. Sun, J.L. Chen, Y.X. Zheng, X. Du, X. G. Hao, Electrochemically switched ion exchange device with serpentine flow field for selective extraction of lithium, *CIESC J.* 74 (5) (2023) 2022–2033. (in Chinese)
[10] Q. Wu, X.F. Liu, M.P. Zheng, Z. Nie, J.J. Yu, Present situation, existing problems and countermeasures of development of salt lake lithium resources in China, *Mod. Chem. Ind.* 37 (5) (2017) 1–5. (in Chinese)
[11] Y. Zhang, Y.H. Hu, L. Wang, W. Sun, Systematic review of lithium extraction from salt-lake brines *via* precipitation approaches, *Miner. Eng.* 139 (2019) 105868.
[12] X.R. Lai, P. Xiong, H. Zhong, Extraction of lithium from brines with high Mg/Li ratio by the crystallization–precipitation method, *Hydrometallurgy* 192 (2020) 105252.
[13] G.Y. Tian, J. Gao, M.R. Wang, X.T. Wen, Y.T. Liu, J. Xiang, L. Zhang, P.G. Cheng, J. P. Zhang, N. Tang, Structural stabilization of Cr-doped spinel $LiMn_2O_4$ for long-term cyclability towards electrochemical lithium recovery in original brine, *Electrochim. Acta* 475 (2024) 143361.
[14] Z. Li, K. Binnemans, Selective removal of magnesium from lithium-rich brine for lithium purification by synergic solvent extraction using β-diketones and Cyanex 923, *AIChE J.* 66 (7) (2020) e16246.
[15] B.H. Chen, Y. Guo, X.H. Zhang, G.Q. Yu, Deep eutectic solvent-assisted selective extraction of valuable metals from waste lithium-ion batteries, *AIChE J.* 70 (5) (2024) e18394.
[16] X.F. Li, X. Li, G.J. Chen, H. Li, Y. Duan, Y. Sun, A. Tiraferri, B.C. Liu, Efficient recovery of lithium from spent lithium-ion battery raffinate by Mn and Al-based adsorbents: pretreatment, adsorption mechanism, and performance comparison, *Sep. Purif. Technol.* 354 (2025) 128652.
[17] J. Chen, J.Q. Jin, J.G. Yu, S. Lin, Adsorption weakening mechanism and regulation strategy of aluminum-based lithium adsorbents in carbonate-style brines, *AIChE J.* 70 (8) (2024) e18463.

[18] L. Zhang, M.Y. Hu, B.Q. He, H.C. Pei, X.H. Li, H. Matsuyama, A review of the nanofiltration membrane for magnesium and lithium separation from salt-lake brine, *Sep. Purif. Technol.* 354 (2025) 129169.
[19] B.W. Hou, R. Fu, H.Y. Wang, J.Y. Yan, R.R. Li, B.Y. Wang, C.X. Jiang, Y.M. Wang, T. W. Xu, One-step conversion of sulfate lithium into high-purity lithium hydroxide crystals *via* bipolar membrane crystallization, *AIChE J.* 69 (11) (2023) e18208.
[20] Z.J. Qin, X.H. Li, X.J. Shen, Y. Cheng, F.X. Wu, Y.J. Li, Z.J. He, Electrochemical selective lithium extraction and regeneration of spent lithium iron phosphate, *Waste Manag.* 174 (2024) 106–113.
[21] W.G. Zhu, W.H. Xu, D.F. Liu, L.H. He, X.H. Liu, Z.W. Zhao, Ionic transport kinetics of selective electrochemical lithium extraction from brines, *Electrochim. Acta* 475 (2024) 143519.
[22] H.Y. Zhang, B.G. Zhang, B. Ai, K.F. Pan, W.M. Zhang, L.P. Zhang, Z.N. Shi, Direct electrochemical extraction of metallic Li from a molecular liquid–based electrolyte under ambient conditions, *Electrochim. Acta* 441 (2023) 141845.
[23] Y. Jang, C.H. Hou, S. Park, K. Kwon, E. Chung, Direct electrochemical lithium recovery from acidic lithium-ion battery leachate using intercalation electrodes, *Resour. Conserv. Recycl.* 175 (2021) 105837.
[24] R.Q. Li, Y.J. Li, L.P. Dong, Q. Yang, S.C. Tian, Z.Q. Ren, Z.Y. Zhou, Study on selective recovery of lithium ions from lithium iron phosphate powder by electrochemical method, *Sep. Purif. Technol.* 310 (2023) 123133.
[25] C. Wang, X. Du, F.F. Gao, X.G. Hao, G.Q. Guan, Electrochemically switched ion separation technologies: a review on electroactive ion exchange materials and system architectures, *Chem. Eng. J.* 490 (2024) 151708.
[26] J. Wang, X. Du, X.Q. Hao, J.H. Luo, X.G. Hao, Q. Cao, G.Q. Guan, J. Li, Z. Liu, Y.G. Li, A. Abudula, A novel photo-assisted electrochemically switched ion exchange technology for selective recovery of bromide ions, *Chem. Eng. J.* 427 (2022) 131693.
[27] J.J. Niu, W.J. Yan, X.Y. Song, W.W. Ji, Z.D. Wang, X.G. Hao, G.Q. Guan, An electrically switched ion exchange system with self-electrical-energy recuperation for efficient and selective LiCl separation from brine lakes, *Sep. Purif. Technol.* 274 (2021) 118995.
[28] Q. Chai, B. Yang, X.M. Li, F.F. Gao, X.G. Hao, A self-driven $Ni(OH)_2$/CB/PVDF film for highly efficient adsorption of tungsten *via* hydroxyl ligand exchange, *Sep. Purif. Technol.* 352 (2025) 128163.
[29] Z. Li, X. Song, W.K. Li, X.L. Ding, L.J. Li, M.J. Liu, L.H. Zhang, C.T. Zhu, Z.C. Chen, A novel high-performance IIP@PPy/rGO@PVDF composite membrane for the selective recovery of lithium-ion *via* an external-voltage-driven process, *Sep. Purif. Technol.* 354 (2025) 129581.
[30] D. Zhang, P.L. Zhang, D. Xiao, X.G. Hao, Investigation of a novel high-efficiency ion-permselective membrane module based on the electrochemically switched ion exchange scheme, *RSC Adv.* 11 (35) (2021) 21248–21258.
[31] W.B. Ma, G.J. Han, J. Li, X.W. An, F.F. Gao, X. Du, J. Li, Z. Liu, G.Q. Guan, X.G. Hao, Hierarchical electroactive ion permselective membrane with electrochemical switched ion pump effect for continuous lithium-ion recovery, *J. Membr. Sci.* 700 (2024) 122719.
[32] X.F. Zhang, J. Wang, Z.L. Zhang, X. Du, F.F. Gao, X.G. Hao, A. Abudula, G.Q. Guan, Z. Liu, J. Li, Modelling of pseudocapacitive ion adsorption of electrochemically switched ion exchange based on electroactive site concentration, *Sep. Purif. Technol.* 286 (2022) 120451.
[33] G.L. Zeng, D.N. Ye, X.F. Zhang, F.F. Gao, X.G. Hao, J. Li, Z. Liu, A potential-responsive ion-pump system based on nickel hexacyanoferrate film for selective extraction of cesium ions, *Chin. J. Chem. Eng.* 63 (2023) 51–62.
[34] D.N. Ye, F.F. Gao, G.L. Zeng, X.F. Zhang, X.G. Hao, J. Li, Z. Liu, Z.Y. Ji, An electroactive BiOBr/PVDF/CB film electrode for electrochemical extraction of bromine ions from brines, *Ind. Eng. Chem. Res.* 62 (22) (2023) 8882–8892.
[35] J.Z. Yu, D.L. Fang, H. Zhang, Z.Y. Leong, J.T. Zhang, X.X. Li, H.Y. Yang, Ocean mining: a fluidic electrochemical route for lithium extraction from seawater, *ACS Mater. Lett.* 2 (12) (2020) 1662–1668.
[36] Y. Sano, X.H. Bai, S. Amagai, A. Nakayama, Effect of a porous spacer on the limiting current density in an electro-dialysis desalination, *Desalination* 444 (2018) 151–161.
[37] C. Mahendra, P.M. Satya Sai, C. Anand Babu, Current–voltage characteristics in a hybrid electrodialysis–ion exchange system for the recovery of cesium ions from ammonium molybdophosphate-polyacrylonitrile, *Desalination* 353 (2014) 8–14.
[38] H.J. Lee, H. Strathmann, S.H. Moon, Determination of the limiting current density in electrodialysis desalination as an empirical function of linear velocity, *Desalination* 190 (1–3) (2006) 43–50.
[39] K.J. Min, E.J. Oh, G. Kim, J.H. Kim, J.H. Ryu, K.Y. Park, Influence of linear flow velocity and ion concentration on limiting current density during electrodialysis, *Desalin. Water Treat.* 175 (2020) 334–340.
[40] S.L. Liao, C.F. Xue, Y.H. Wang, J.L. Zheng, X.G. Hao, G.Q. Guan, A. Abuliti, H. Zhang, G.Z. Ma, Simultaneous separation of iodide and cesium ions from dilute wastewater based on PPy/PTCF and NiHCF/PTCF electrodes using electrochemically switched ion exchange method, *Sep. Purif. Technol.* 139 (2015) 63–69.
[41] B. Sun, X.G. Hao, Z.D. Wang, Z.L. Zhang, S.B. Liu, G.Q. Guan, Continuous separation of cesium based on NiHCF/PTCF electrode by electrochemically switched ion exchange, *Chin. J. Chem. Eng.* 20 (5) (2012) 837–842.
[42] Z.R. Zhang, B.L. Chen, H. Zhang, Y.M. Wang, C.X. Jiang, T.W. Xu, Numerical simulation of ion transport across monovalent ion perm-selective membranes, *Chem. Eng. Sci.* 264 (2022) 118193.
[43] Z.R. Zhang, F.B. Luo, C.X. Jiang, T.W. Xu, Power-free bipolar membrane electrodialysis for acid–alkali production in river estuaries, *Chem. Eng. Sci.* 273 (2023) 118643.
[44] M. Tedesco, H.V.M. Hamelers, P.M. Biesheuvel, Nernst-Planck transport theory for (reverse) electrodialysis: I. Effect of co-ion transport through the membranes, *J. Membr. Sci.* 510 (2016) 370–381.
[45] A. Campione, L. Gurreri, M. Ciofalo, G. Micale, A. Tamburini, A. Cipollina, Electrodialysis for water desalination: a critical assessment of recent developments on process fundamentals, models and applications, *Desalination* 434 (2018) 121–160.
[46] T.F. Fuller, M. Doyle, J. Newman, Simulation and optimization of the dual lithium ion insertion cell, *J. Electrochem. Soc.* 141 (1) (1994) 1–10.
[47] X.F. Zhang, Z. Zhang, L. Xing, J. Xuan, X.G. Hao, F.F. Gao, X. Du, Z.L. Zhang, X.W. An, G.Q. Guan, Z. Liu, Modelling and optimization of Li^+ extraction from brine with high Mg/Li ratio by electrochemically switched ion exchange considering thermodynamics and dynamics simultaneously, *Chem. Eng. J.* 481 (2024) 148625.
[48] V.C.E. Romero, M. Tagliazucchi, V. Flexer, E.J. Calvo, Sustainable electrochemical extraction of lithium from natural brine for renewable energy storage, *J. Electrochem. Soc.* 165 (10) (2018) A2294–A2302.
[49] V.C.E. Romero, D.S. Putrino, M. Tagliazucchi, V. Flexer, E.J. Calvo, Sustainable electrochemical extraction of lithium from natural brine: part II. Flow reactor, *J. Electrochem. Soc.* 168 (2) (2021) 020518.
[50] Z.Y. Geng, S.Y. Wang, M.J. Lacey, D. Brandell, T. Thiringer, Bridging physics-based and equivalent circuit models for lithium-ion batteries, *Electrochim. Acta* 372 (2021) 137829.
[51] J.W. Su, G.L. Chai, L. Wang, W.D. Cao, Z.L. Gu, C.G. Chen, X.Y. Xu, Pore-scale direct numerical simulation of particle transport in porous media, *Chem. Eng. Sci.* 199 (2019) 613–627.
[52] B. Alazmi, K. Vafai, Analysis of fluid flow and heat transfer interfacial conditions between a porous medium and a fluid layer, *Int. J. Heat Mass Tran.* 44 (9) (2001) 1735–1749.